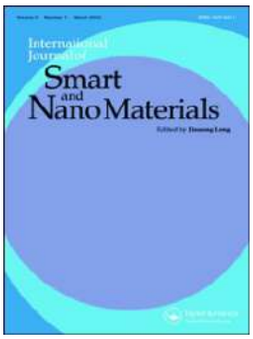

International Journal of Smart and Nano Materials

ISSN: (Print) (Online) Journal homepage: https://www.tandfonline.com/loi/tsnm20

A bio-inspired 3D metamaterials with chirality and anti-chirality topology fabricated by 4D printing

Wei Zhao, Jie Zhu, Liwu Liu, Jinsong Leng & Yanju Liu

To cite this article: Wei Zhao, Jie Zhu, Liwu Liu, Jinsong Leng & Yanju Liu (2023) A bio-inspired 3D metamaterials with chirality and anti-chirality topology fabricated by 4D printing, International Journal of Smart and Nano Materials, 14:1, 1-20, DOI: 10.1080/19475411.2022.2120110

To link to this article: https://doi.org/10.1080/19475411.2022.2120110

INTERNATIONAL JOURNAL OF SMART AND NANO MATERIALS
2023, VOL. 14, NO. 1, 1–20
https://doi.org/10.1080/19475411.2022.2120110

A bio-inspired 3D metamaterials with chirality and anti-chirality topology fabricated by 4D printing

Wei Zhao[a], Jie Zhu[a], Liwu Liu[a], Jinsong Leng[b] and Yanju Liu[a]

[a]Department of Astronautical Science and Mechanics, Harbin Institute of Technology (HIT), Harbin, People's Republic of China; [b]Center for Composite Materials and Structures, Harbin Institute of Technology (HIT), Harbin, People's Republic of China

ABSTRACT

Artificial architected metamaterials equipped with unique mechanical and physical properties that are naturally inaccessible can be obtained by rational design. In this work, the innovative three-dimensional (3D) chiral and anti-chiral metamaterials are developed referring to the face-rotating polyhedral (FRP) structure present in the virus. Through assembling planar triangular units into the regular octahedron cells, several typical forms of chiral and anti-chiral metamaterials can be obtained by different assembly methods. By changing the topology parameters, the Poisson's ratio can be adjusted between [0, 2.8]. The metamaterials are fabricated by 3D printing utilizing shape memory polymer, and the mechanical properties are analyzed via Finite Element Analysis (FEA) and experiments, including Young's modulus, Poisson's ratio, and tension-twist coupling behavior. In addition, target metamaterial with specific local deformation behavior is obtained by programmatic calculations and distributions to meet special requirements or achieve unique applications. The shape memory property endows the mechanical metamaterials with more potential applications.

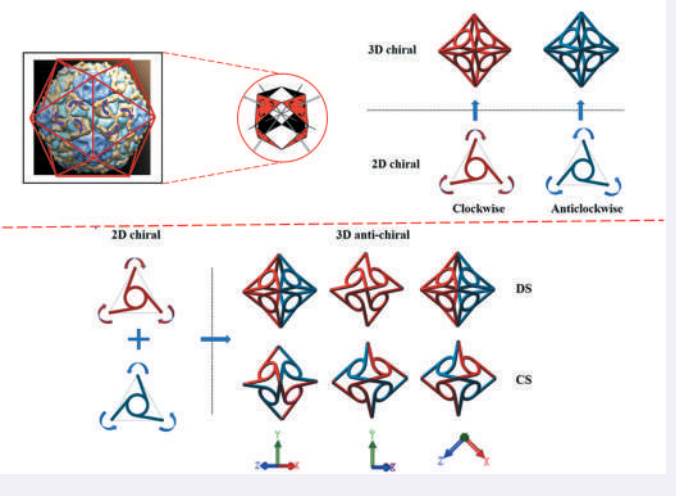

ARTICLE HISTORY
Received 29 April 2022,
Accepted 26 August 2022

KEYWORDS
3D assembly; tension-twist coupling; chiral and anti-chiral; metamaterials; shape memory

CONTACT Yanju Liu yj_liu@hit.edu.cn Department of Astronautical Science and Mechanics, Harbin Institute of Technology (HIT), No. 92 West Dazhi Street, Harbin 150001, People's Republic of China
Supplemental data for this article can be accessed online at https://doi.org/10.1080/19475411.2022.2120110

1. Introduction

With the rational design of artificial architected metamaterials, unique mechanical and physical properties that are inaccessible in the natural world can be obtained. The main core in all metamaterials comprises fabricating a medium composed of repeating unit cells at a scale that is smaller than the wavelength of interest, giving rise to the smart properties of metamaterials. These inter-unit cells acting as artificial atoms interact with electromagnetic radiation, sound and optical waves, causing them to block, absorb, intensify, or bend. Potential applications of metamaterials are diverse, including metamaterial antennas [1–3], metamaterial absorbers [4–6], metamaterial cloaking devices [7–9], and metamaterial sound filtering [10–12], etc. Auxetic metamaterials, known as a special type of mechanical metamaterials, exhibit a negative Poisson's ratio property, as they can expand (contract) in a transverse direction when uniaxially stretched (compressed) [13–16]. Besides, auxetic metamaterials also show some other unique characteristics, including higher shearing modulus, higher fracture toughness and excellent absorption properties [17–21].

According to the geometric configuration of the auxetic unit cell, auxetic metamaterials can be divided into three types including reentrant structures, rigid square rotation structures and chiral structures [22]. If a structure can be distinguished from its mirror image, it can be called a chiral structure. Chirality is an omnipresent phenomenon in nature, existing on microscopic, millimeter, and macroscopic scales. For example, DNA is in a right-hand helix, called B form DNA, quartz is a chiral structure at the interatomic level including left-handed and right-handed, and both left-handed and right-handed snail shells exist in nature. Furthermore, scientists have designed and fabricated an assortment of artificial chiral metamaterials to meet different needs.

A series of planar chiral metamaterials have been designed, such as hexagonal chiral metamaterial, trigonal chiral metamaterial and tetragonal chiral metamaterial. Their mechanical properties including bulk modulus and negative Poisson's ratio have been explored [23,24]. With the advances in manufacturing technology, scientists have introduced the chirality concept into the design of 3D metamaterials [25–27]. Qi et al. [28] developed a kind of novel 3D chiral metamaterials by designing the lattice, and a series of chiral structures were obtained by changing the topological. Mizzi et al. [29] have conducted a large number of studies on chiral metamaterials. Based on the uniform Euclidean tessellations, they developed a series of chiral metamaterials with auxetic properties. The effect of the topological parameter on the mechanical structure was investigated. By this method, they were able to transform materials with complex shapes into metamaterials with negative auxetic properties. Further, Mizzi et al. [30] present a novel design method for metamaterials based on the octagon and dodecagon elements. These designs demonstrate the great potential of the Euclidean polygonal tessellations method in the design of metamaterial. Tarnai et al. [31] investigated the mechanical properties of symmetry reasoning, which provide a theoretical reference for the design of auxetics structures.

By reasonable design, 3D chiral metamaterials can be endowed with more functions including tension-twist coupling behavior and size effect which cannot be harvested in planar chiral metamaterials. These unique properties endow 3D chiral metamaterials with more application potentials in morphing airfoil smart deployable antenna, reconfigurable

structures, auxetic stent, chiral flexible electronics and optical dynamic cloaking structures [32,33].

However, most of the 3D chiral structures are constructed directly. Few have been assembled by using the two dimensions (2D) chiral structures, which will undoubtedly increase the difficulty in the design of 3D chiral metamaterials. Consequently, referring to our previous work on 2D chiral structures [34], trying to realize the transference of chirality from 2D to 3D is the primary work in this paper. In chemistry, scientists have worked out to synthesize chiral molecular polyhedral through the self-assembly of planar chiral molecular [35,36]. The same method of face-rotating polyhedral (FRP) can be used to design 3D chiral structures and 3D anti-chiral structures, which will greatly shorten the design period. In this work, the structures are fabricated by 3D printing [37–39] using shape memory polymer [40–44] and have the advantages of easy assembly, high flexibility and shape memory properties. Further, the mechanical behaviors of the proposed chiral and anti-chiral metamaterials are studied by experiments and Finite Element Analysis (FEA). The transference of chirality from 2D to 3D proves to be feasible and functional, thus it opens a new door for the design of 3D chiral metamaterials.

2. Design of 3D chiral and anti-chiral metamaterials

The structure layout of a basic planar chiral unit is shown in Figure 1(a), and the design of this structure is completed based on our previous work [34]. The triangular representative volume element comprises three ligaments and one ring that connects the three ligaments. The ligaments are tangents to the circle, and the angle between the ligaments and the connecting lines of the joint center is denoted as θ. The length of the imaginary triangle is a, the radius of the center node of the triangle is denoted as r with a wall thickness of d_r, and the length of the ligament is denoted as l with a wall thickness of d_l. In addition, the thickness of the whole unit is denoted as d. The geometry parameters are connected by the following relations:

$$\sin|\theta| = \frac{\sqrt{3}r}{3a}, \cos\theta = \frac{\sqrt{3}l}{3a} \tag{1}$$

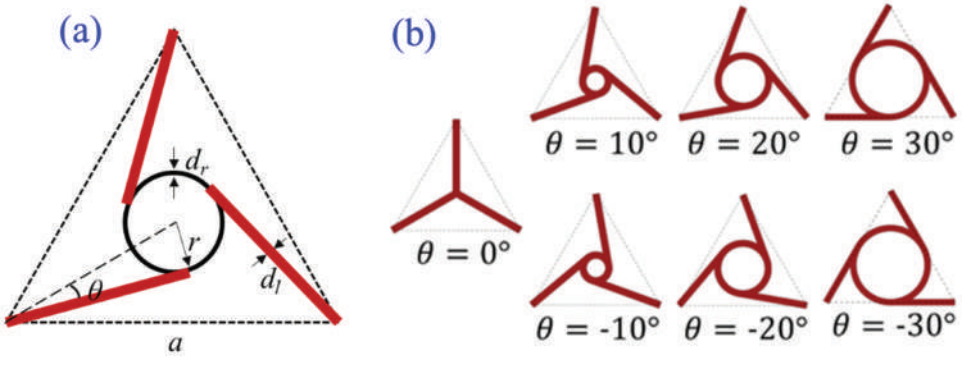

Figure 1. Configuration of the basic planar unit (a) Definition of the geometry parameters (b) Unit with different topology angle θ.

The different geometry configurations of the basic planar chiral unit can be obtained by changing the topology parameter of θ as illustrated in Figure 1(b). θ can take different values ranging from -30° to 30°, and the unit displays right-rotational property when θ is positive while displays left-rotational when θ is negative. However, the chirality of the unit disappears when θ equals zero.

The schematic diagram of the FRP structure is illustrated in Figure 2(a), which is derived from the icosahedral cricket paralysis virus. By rotating each face of the polyhedron around its central axis, the transference of chirality from the faces to the polyhedron can be achieved. Using this method, chemists have synthesized chiral molecular polyhedral through the self-assembly of planar chiral molecular [35,36]. Inspired by the fascinating methods, the proposed planar chiral units are used to assemble the regular octahedron cell.

Different units and assembly methods can produce different structures as illustrated in Figure 2(b,c). The regular octahedron cell displays right-rotation when the eight planar units are clockwise while it displays left-rotational when they are anticlockwise. If the regular octahedron cell is assembled by four clockwise and four anti-clockwise units, it can display anti-chirality, such as DS (Diagonal Symmetry) and CS (Central Symmetry) as illustrated in Figure 2(c). Structure DS is assembled by anti-chiral cells, which are diagonal symmetry and the unit cells of different rotations are located on the different sides of the

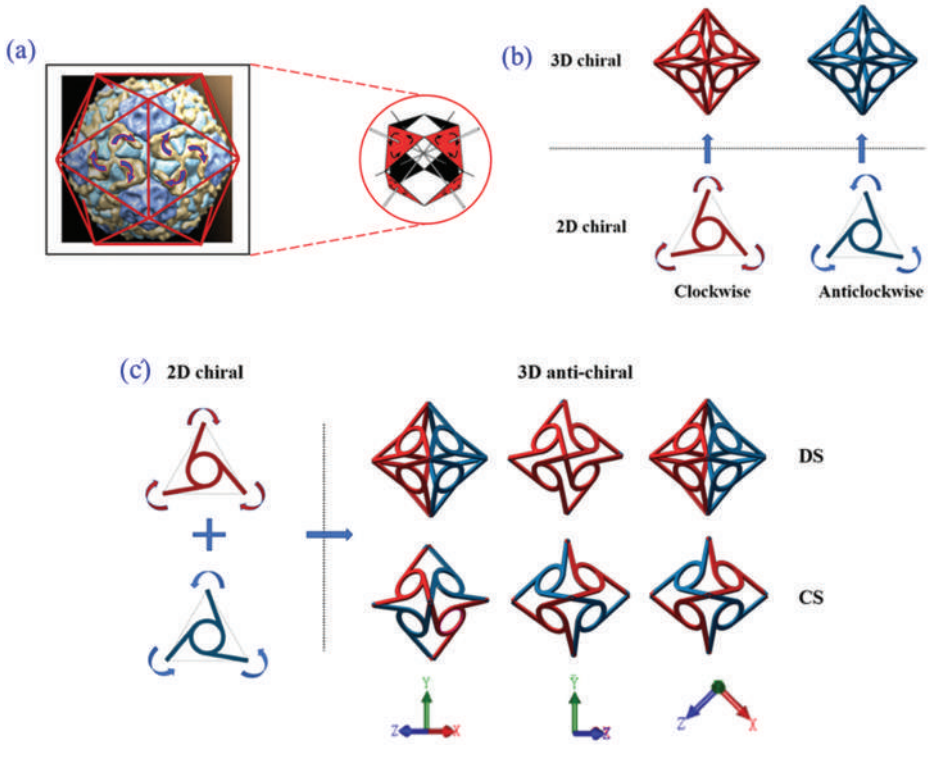

Figure 2. (a) Design prototype of 3D chiral structure (b) Assembly of 2D chiral units to the 3D chiral structure inspired by the icosahedral cricket paralysis virus (c) Assembly of 2D chiral units to 3D anti-chiral structure, including DS and CS.

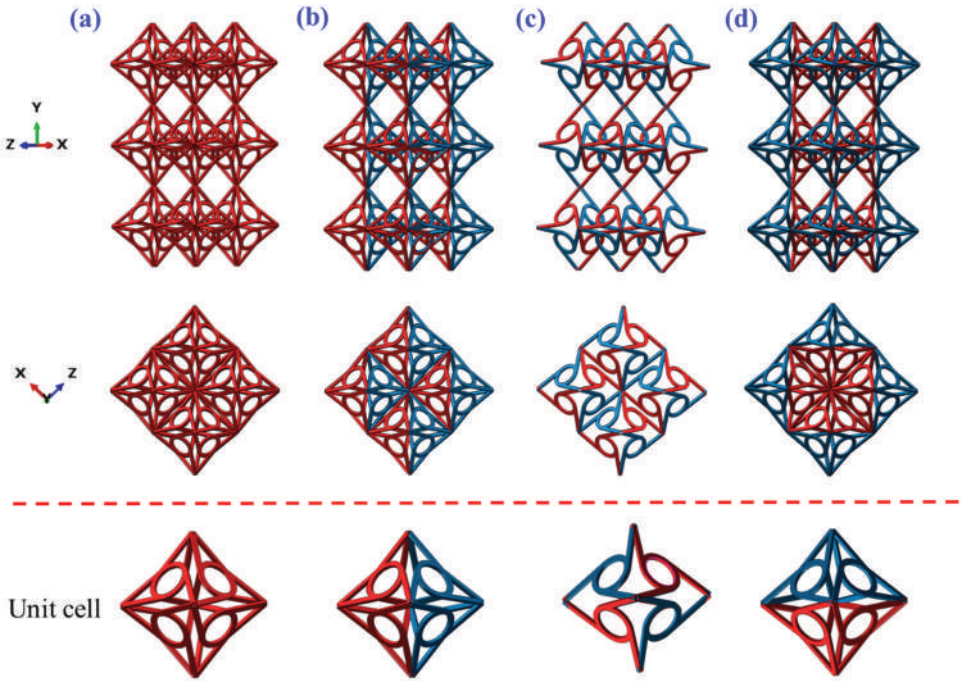

Figure 3. (a) Original chiral metamaterial (b) DS anti-chiral metamaterial (c) CS anti-chiral metamaterial (d) DS chiral metamaterial.

diagonal. Structure CS is central symmetry as the regular octahedron has units with different rotation directions on two planes of central symmetry.

By assembling these chiral or anti-chiral regular octahedron cells, the 3D metamaterials can be obtained. Several typical assembly methods are illustrated in Figure 3. By assembling with the same kind of chiral cells, the metamaterial displays original chiral characteristics, as shown in Figure 3(a). However, the structures are symmetric and display no chirality (DS and CS anti-chiral metamaterial) when assembled from diagonal symmetric cells or central symmetric cells with the same repeating pattern as shown in Figure 3(b,c). The metamaterial named DS chiral can be obtained with diagonal symmetric cells as shown in Figure 3(d). In the horizontal plane, rotating the adjacent four octahedron cells for 0°, 90°, 180° and 270° will enable the same rotation direction of the units in octahedron cells to face the central axis, thus making the entire structure present chirality behavior.

3. Mechanical behaviors of the 3D chiral and anti-chiral metamaterials

3.1. Materials and manufacturing

The 3D chiral and anti-chiral metamaterials were fabricated by a photocuring 3D printer (Anycubic Photon). The photosensitive resin was provided by Prof. Leng's group-the Center for Smart Materials and Structure, Harbin Institute of Technology (HIT). The specimen was fabricated with a bottom exposure time of 80s and a normal exposure time of 23s, and the spatial resolution was 0.1 mm.

Dynamic thermomechanical analysis (DMA) was used to test the storage modulus and loss angle *tan δ* changing with temperature as shown in Figure 4(a). When the temperature was 25°C, the storage modulus was 1296 MPa while the temperature was 90°C, the storage modulus was 19 MPa. Taking the peak value of *tan δ* curve as the glass transition temperature (T_g), it can obtain T_g = 62°C. The Zwick-010 universal tensile machine was used to test the tensile properties of SMP at different temperatures as shown in Figure 4 (b). The specimen was prepared according to the standard of ASTM D638 with the dimension of 115 mm × 65 mm × 3 mm. The uniaxial tensile tests were carried out with

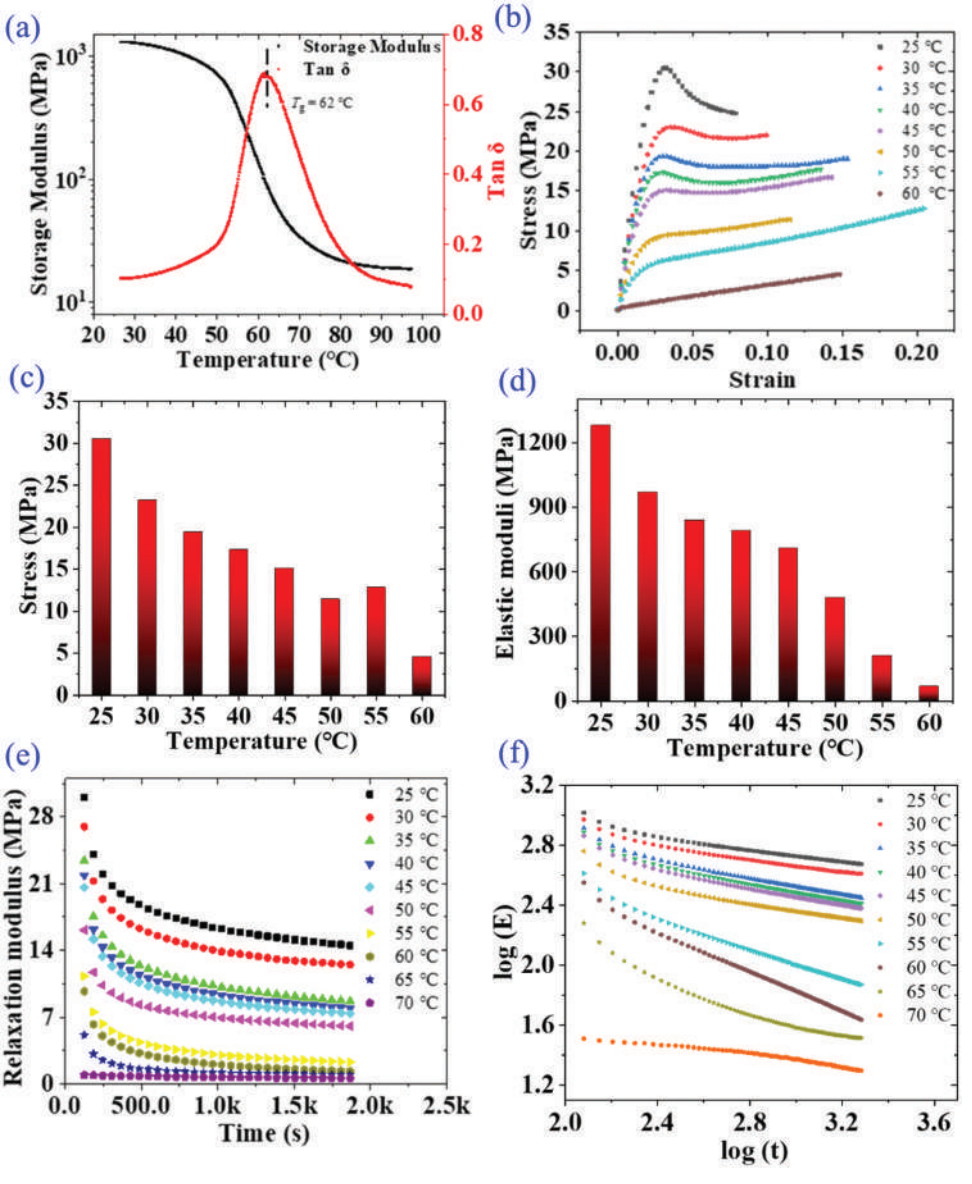

Figure 4. Mechanical properties of SMP (a) DMA test (b) Uniaxial tensile tests (c) Stress vs. Temperatures (d) Elastic moduli vs. Temperatures (e) Relaxation modulus vs. Time (f) Log E vs. log t.

a loading rate of 2 mm/min. When the temperature was 25°C, the tensile strength was 30 MPa, and when the temperature was 60°C, the tensile strength was 4.5 MPa as shown in Figure 4(c). With the increase of temperature, the elastic modulus decreased from 1280 MPa at 25°C to 66 MPa at 60°C as shown in Figure 4(d).

Since SMP is a viscoelastic material, the mechanical properties are not only dependent on time, but also change with temperature. The relaxation experiments were conducted to investigate the viscoelastic of SMP. The specimen was applied 2 mm deformation with a loading rate of 1 mm/min and then kept the deformation for 1800 s. The relaxation moduli–time curve and the log E and log t curves are shown in Figure 4(e,f).

3.2. Mechanical properties of the structures

The metamaterial fabricated by 3D printing is shown in Figure 5. For the structure with topology parameter 0°, the metamaterials display no chirality as shown in Figure 5(a,b) and Figure 5(e) display the chiral metamaterials assembled from chiral cells and diagonal symmetric cells with different topology parameters θ (10, 20 and 30 degrees), respectively. Figure 5(c,d) exhibit anti-chiral metamaterials assembled from diagonal symmetric cells and central symmetric cells of different topology parameters θ (10°, 20° and 30°), respectively. The unit cells painted with red are right-rotational units while those painted

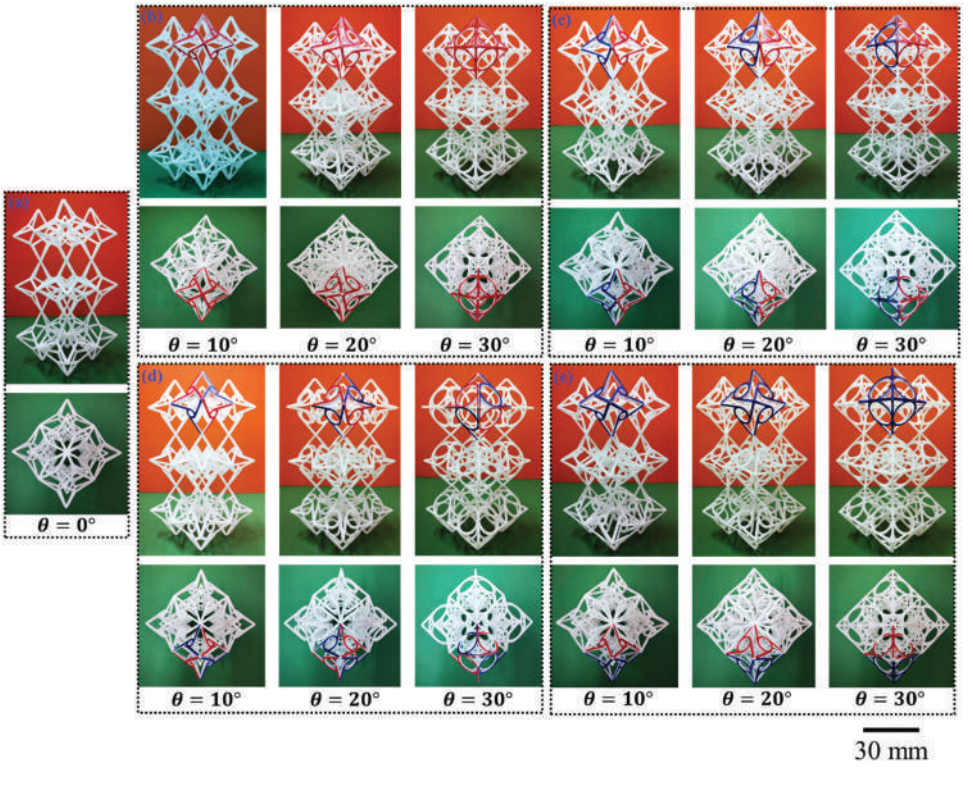

Figure 5. Front view and top view of the metamaterial (a) Assembled from chiral cells with 0° (b) Original chiral metamaterial (c) DS anti-chiral metamaterial (d) CS anti-chiral metamaterial (e) DS chiral metamaterial.

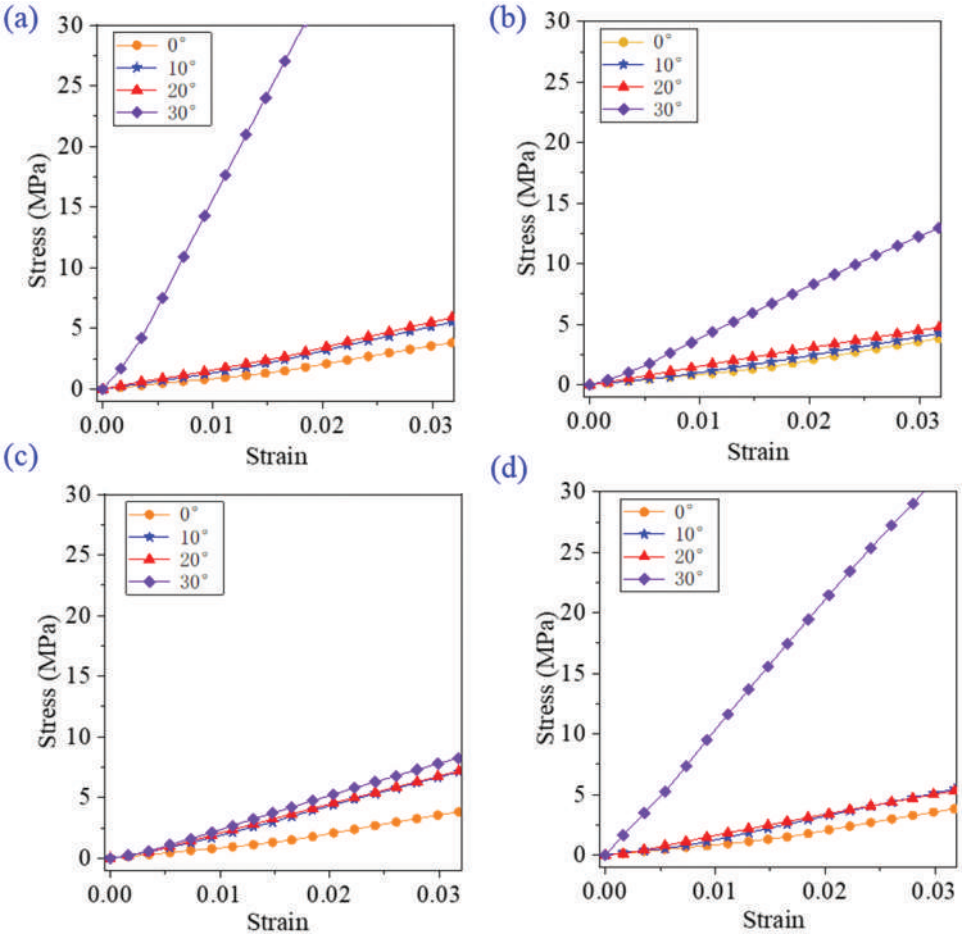

Figure 6. Stress σ vs. strain ε under axial compression (a) Original chiral metamaterial (b) DS anti-chiral metamaterial (c) CS anti-chiral metamaterial (d) DS chiral metamaterial.

with blue represent the units with the property of left-rotation (more clearer images can be found in Supporting Information, Figure S1).

The mechanical properties of the chiral and anti-chiral metamaterials were studied by experiments with a loading rate of 2 mm/min. Figure 6 illustrates the relationship between stress and strain of the four types of metamaterials during uniaxial compression. In addition, the displacement and deformation images that are recorded during compression are described in Figure 7 (Images of the magnified unit cells can be found in Supporting Information, Figure S2). All of the structures are applied a strain of 0.032.

3.3. Finite element analysis

In this work, the Generalized Maxwell model was established and implemented by ABAQUS to investigate the mechanical properties. The schematic is shown in Figure 8, which consisted of multiple Maxwell elements connected in parallel. Each Maxwell

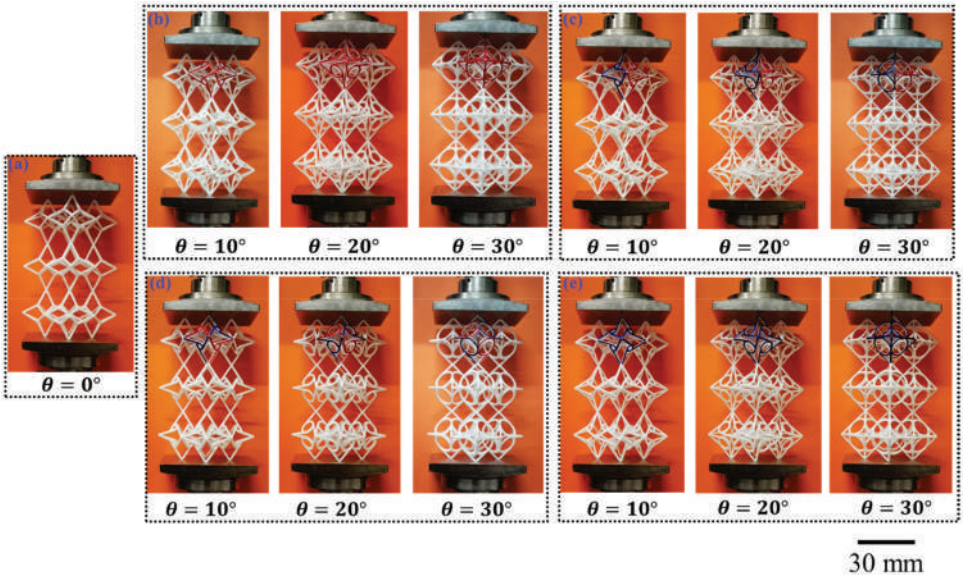

Figure 7. Axial compression test of metamaterial (a) Assembled from chiral cells with 0° (b) Original chiral metamaterial (c) DS anti-chiral metamaterial (d) CS anti-chiral metamaterial (e) DS chiral metamaterial.

element included an elastic element with an elastic modulus of E_i and a viscous element with the viscosity of η_i.

This model can intuitively reflect the stress relaxation law of SMP, and its constitutive equation can be expressed as:

$$\sigma(t) = \left(E_{s_0} + \sum_{i=1}^{n} \frac{E_{s_i} d/dt}{d/dt + 1/\tau_i}\right)\varepsilon(t) \tag{2}$$

where $\sigma(t)$ is the stress changing with time, E_{s_i} is relaxation function, E_{s_0} is the initial modulus, n indicates the number of Maxwell elements, $\tau_i = \frac{\eta_i}{E_i}$ is the relaxation time of i^{th} Maxwell element in the model. When the step strain ε_0 is applied, the Prony series expression of the stress relaxation modulus is:

$$E_s = E_{s0} + \sum_{i=1}^{n} E_{si} + exp(-t/\tau_i) \tag{3}$$

When $t \to 0$, it can be obtained $E(0) = E_{s_0} + \sum_{i=1}^{n} E_{s_i}$. For SMP, the effect of time and temperature on viscoelastic behavior is obvious, and the effects of time and temperature on the viscoelastic behavior of SMP are equivalent. The introduction of the temperature shift factor α_T relates to the influence of time and temperature on viscoelastic behavior.

$$\log E(\log t,\ T_s) = \log E(\log t - \log \alpha_T,\ T_m) \tag{4}$$

The relaxation modulus at each temperature is converted to T_s to realize superposition so that the stress relaxation modulus curve at temperature T_s has a wider time range.

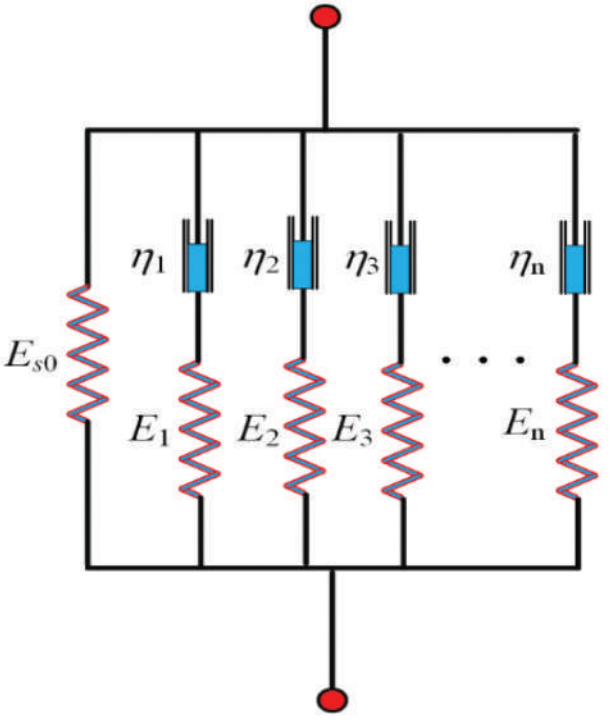

Figure 8. Schematic of GMM model.

According to the Williams–Lamdel–Ferry (WLF) equation [44], the expression can be expressed as:

$$\log a_T = \frac{-C_1(T - T_m)}{C_2 + (T - T_m)} \tag{5}$$

where C_1 and C_2 are materials parameters, and T_m is reference temperature.

In this section, the mechanical behaviors of the 3D chiral and anti-chiral metamaterials under uniaxial compression were analyzed via Finite Element Analysis and experiments. The model parameters implanted into ABAQUS is shown in Table 1.

The metamaterials containing a sufficient number of cells can be regarded as a continuum. Simplifying the deformation of chiral metamaterial into the displacements of the unit cell, the strain of 3D chiral and anti-chiral meta materials can be obtained by combining with the concept of average strain. As illustrated in Figure 9, the original chiral metamaterial is developed with right-rotational regular octahedron

Table 1. Model parameters implanted into ABAQUS.

Physical meaning	Symbol	Value
Viscoelastic parameters	g_1, g_2, g_3, g_4, g_5, g_6	0.87, 0.06, 0.05, 0.004, 0.007, 0.0001
Elastic parameter	τ_1, τ_2, τ_3, τ_4, τ_5, τ_6	0.1, 1, 10, 100, 1000, 10,000
WLF parameters	C_1, C_2, T_m	16.64, 48.6, 52°C
Coefficients of thermal expansion	α	0.000117 ($<T_g$) 0.000235 ($>T_g$)

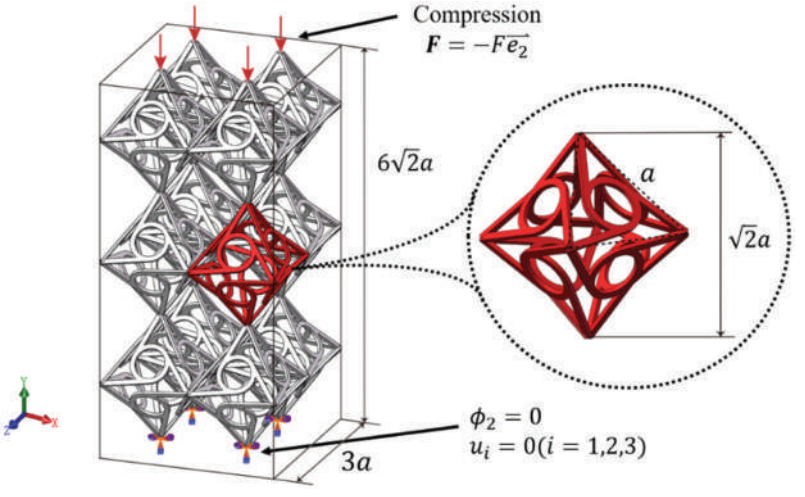

Figure 9. The FEA model of the original chiral metamaterial (ϕ_2 means that the rotational degree of freedom along the Y-axis is 0).

cells. To simplify the parameters, the length–width ratio of the ligaments is defined as $\eta = t_l/l$.

To study its mechanical properties, the finite element models of the proposed metamaterial are employed for simulation. Finite element simulations are performed for metamaterials with different topology parameters θ (-30 degrees through 30 degrees) and different assembly methods (including original chiral metamaterial, DS anti-chiral metamaterial, CS anti-chiral metamaterial and DS chiral metamaterial). The ligament length–width ratio η of these metamaterials equals to 0.1. The obtained displacement field of the FE model of the proposed chiral and anti-chiral metamaterials is illustrated in Figure 10. During uniaxial compression, the deformation of the metamaterial is governed by bending deformation of the ligaments and rotation of circular nodes, which is closely related to the topology parameter θ and assembly method. When θ equals to 0, the configuration of these metamaterials is the same and there is no chirality as shown in Figure 10(a). However, when $\theta \neq 0$, the four types of metamaterials proposed display different structures and mechanical properties. Chiral metamaterials, as illustrated in Figure 10(b) and Figure 10(e), will twist when imposed with axial loads, exhibiting a unique property named tension-twist coupling behavior. When θ is positive, both two types of chiral metamaterials twist to the right under compression. For the original chiral metamaterial, the chiral cells with positive values of θ are right-rotational. For DS chiral metamaterial, however, the rotation direction of the units in octahedron cells on the side corresponding to the central axis is right when θ is positive, thus the whole metamaterial is right-rotational dominated. For anti-chiral metamaterials as illustrated in Figure 10(c,d), there is no tension-twist coupling behavior and they will compress as normal materials when axial loads are applied. From the top view of the structures shown in Figure 10, it can be seen that the original chiral metamaterial and the DS chiral metamaterial exhibit an obvious compression-torsion effect. The angle between the square of the dotted line

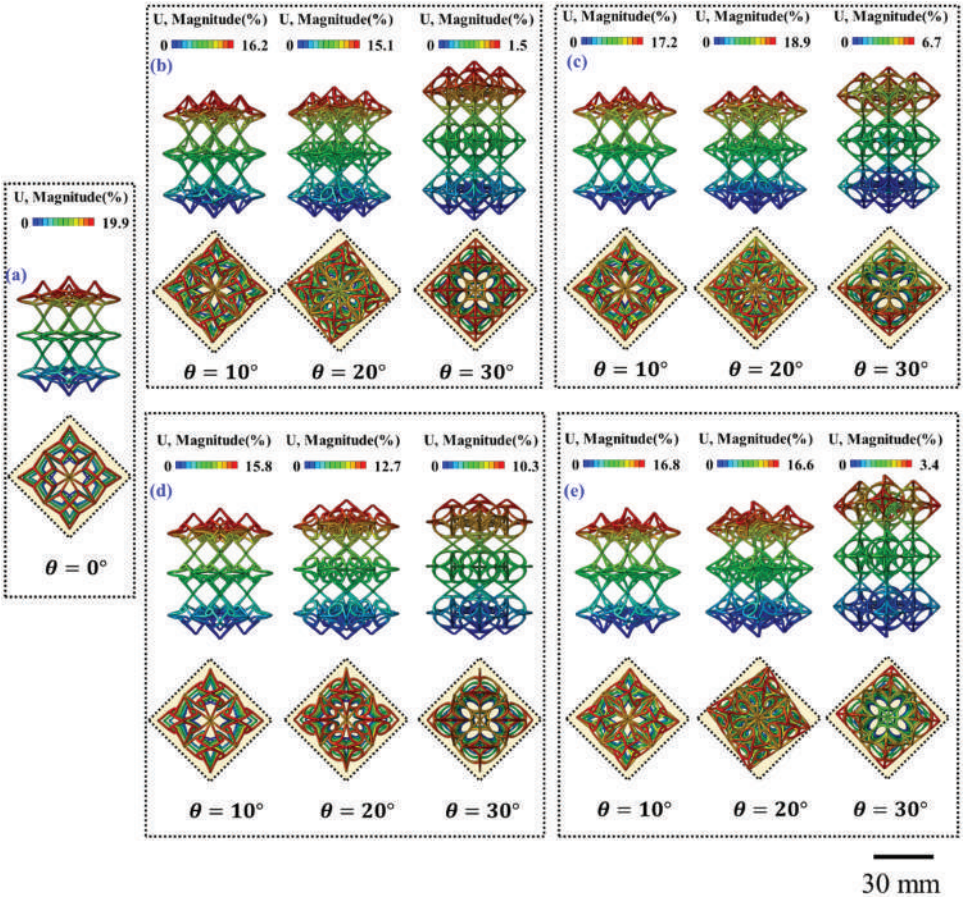

Figure 10. The displacement field of the FE model (a) Assembled from chiral cells with 0° (Strain of 0.16) (b) original chiral metamaterial (Strain of 0.13, 0.12 and 0.01 for structures with θ of 10°, 20°and 30°, respectively) (c) DS anti-chiral metamaterial (Strain of 0.14, 0.15 and 0.05 for structures with θ of 10°, 20°and 30°, respectively) (d) CS anti-chiral metamaterial (Strain of 0.13, 0.10 and 0.08 for structures with θ of 10°, 20°and 30°, respectively) (e) DS chiral metamaterial (Strain of 0.13, 0.13 and 0.03 for structures with θ of 10°, 20°and 30°, respectively).

and the metamaterial represents the magnitude of the twist angle. (Images of the magnified unit cells can be found in Supporting Information S3)

To further study the mechanical properties of the 3D chiral and anti-chiral metamaterials, the metamaterial is regarded as a continuum, and the deformation of the metamaterial is simplified into the displacements of every unit cell. FEA provides the displacements of all nodes in the metamaterial, which can be used to construct the displacement function. With the eight x direction displacements of each face center in a unit cell, the following polynomial can be fitted and the coefficients $m_1 - m_8$ can be determined [27]:

$$u_x = m_1 + m_2x + m_3y + m_4z + m_5xy + m_6yz + m_7xz + m_8xyz \tag{6}$$

Repeating this process in the same way, polynomials of u_y and u_z can be obtained. Furthermore, according to the average strain concept, the strain can be expressed as:

$$\varepsilon_{ij} = \frac{1}{2}\left(\frac{\partial u_i}{\partial x_j} + \frac{\partial u_j}{\partial x_i}\right) \tag{7}$$

where x_1, x_2 and x_3 corresponds to x, y and z in the coordinate system, respectively. By introducing shape functions and matrix $[B]$ for an 8-node brick finite element, the effective strains throughout each unit cell can be calculated by $\{\varepsilon\}=[B]\{d\}$. In addition, the relative Young's Modulus can be expressed as:

$$\frac{E_{eff}}{E_s} = \frac{\frac{\sigma_y}{\varepsilon_y}}{E_s} \tag{8}$$

where E_{eff} is the effective Young's Modulus, and E_s is Young's modulus of the matrix material. Where is E_{eff} the effective Young's Modulus and E_s is the Young's Modulus of the material. Besides, the Poisson's ratio also can be obtained:

$$v_{y_x} = -\frac{\varepsilon_x}{\varepsilon_y}, v_{yz} = -\frac{\varepsilon_z}{\varepsilon_y} \tag{9}$$

4. Results and discussions

In this work, the effective Young's modulus of the metamaterial E_{eff} is normalized by cell wall material's Young's modulus E_s. The comparisons of the relative Young's modulus and Poisson's ratio of the chiral and anti-chiral metamaterials of different topology parameters obtained by experiments and simulations are shown in Figure 11 and Figure 12. Both Young's modulus and Poisson's ratio of the four types of metamaterials are only determined by the absolute value of the topology parameter θ. For the same type of metamaterial, no matter whether θ is positive or negative, the longitudinal and lateral deformation caused by the bending of the ligaments and rotation of the circles is the same. However, different types of metamaterials display different mechanical properties, especially between chiral metamaterials and anti-chiral metamaterials.

From Figure 11, it can be seen that Young's modulus increases with the increase of the absolute value of the topology parameter θ, because the shorter ligaments lead to a smaller bending deformation under the action of the same load. However, when the absolute value θ is about 30 degrees, the relative Young's modulus increases fast to a larger value. Original chiral metamaterial achieves the maximum value, followed by the DS chiral metamaterial, CS anti-chiral metamaterial, and the DS anti-chiral metamaterial. This can be attributed that there are twelve edges of the octahedron cell in the original chiral metamaterial are connected, whereas four in DS chiral metamaterial, two in DS anti-chiral metamaterial and none in CS anti-chiral metamaterial. These connections in the octahedron cell limit the longitudinal deformation of metamaterials, thus decreasing the relative Young's modulus.

The Poisson's ratio changing with respect to the topological angle θ is illustrated in Figure 12. For DS and CS anti-chiral metamaterial, Poisson's ratio decreases with the increase of the absolute value of θ. However, it increases a little of DS anti-chiral metamaterial when θ is about 30 degrees due to deformation limitations of two

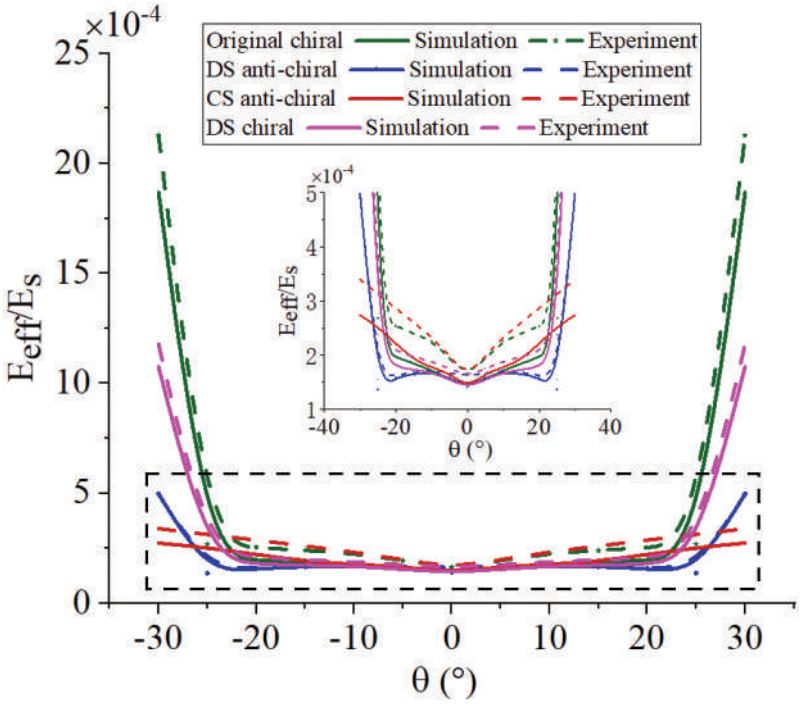

Figure 11. Relative young's modulus $\frac{E_{eff}}{E_s}$ vs. Topology parameter θ.

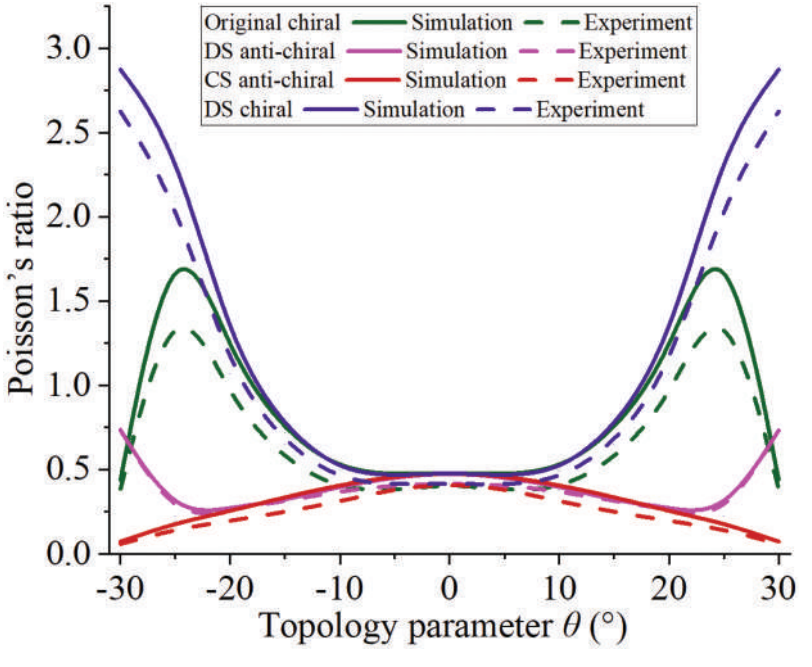

Figure 12. Poisson's ratio v vs. Topology parameter θ.

connected edges. For DS chiral metamaterials, it increases fast with the increase of topology parameter θ and reaches about 3.0 at $\theta = 30^{\circ}$, displaying an enhanced property over anti-chiral metamaterials. In addition, the Poisson ratio of original chiral metamaterial decreases sharply when $\theta = 25^{\circ}$. This can be attributed that the connection of all edges has a constraint effect on the deformation in transverse and longitudinal directions. However, this constraint effect is smaller in chiral metamaterials DS.

The relationships between twist angle/axial strain and topology parameter θ are illustrated in Figure 13. According to the observed experimental results, the twist angle is positive if the metamaterial is twisted to right under compression. This value equals zero in anti-chiral metamaterials DS and CS as there is no chirality behavior. Chiral metamaterials with opposite topology parameters have the same deformation and twist angle in the opposite directions. This tension-twist coupling behavior turns more evident with the increase of topological angle θ. However, for the original chiral metamaterial, the tension-twist coupling behavior disappears when θ is about 30 degrees. It may be attributed that the connection of edges greatly limits its torsion deformation.

According to the different mechanical properties exhibited by the metamaterials, more advanced metamaterials structures can be designed to meet some specific requirements. Local deformation of the target metamaterial can be achieved by controlling the topology parameter or assembling method layer by layer. As shown in Figure 14, the target metamaterial is constructed by six layers of original chiral metamaterial with different topology angles (Images of the magnified unit cells can be found in Supporting Information, Figure S4). From bottom to top, the topological angle θ are 0, 10, 20, −20, −10, 0 degrees, respectively. Further, the relative Young's modulus of this target metamaterial can be calculated as:

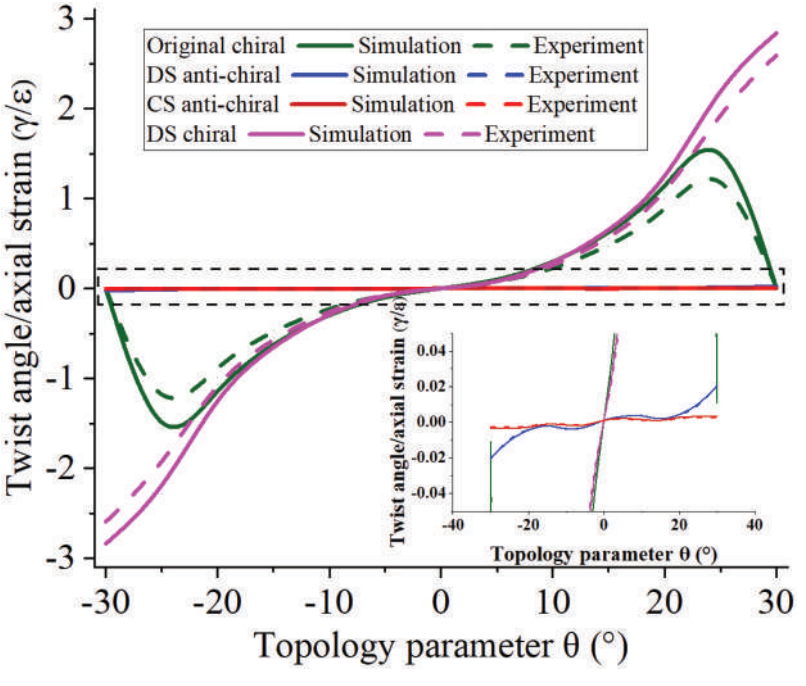

Figure 13. Twist angle/axial strain $\frac{\gamma}{\varepsilon}$ vs. topology parameter θ.

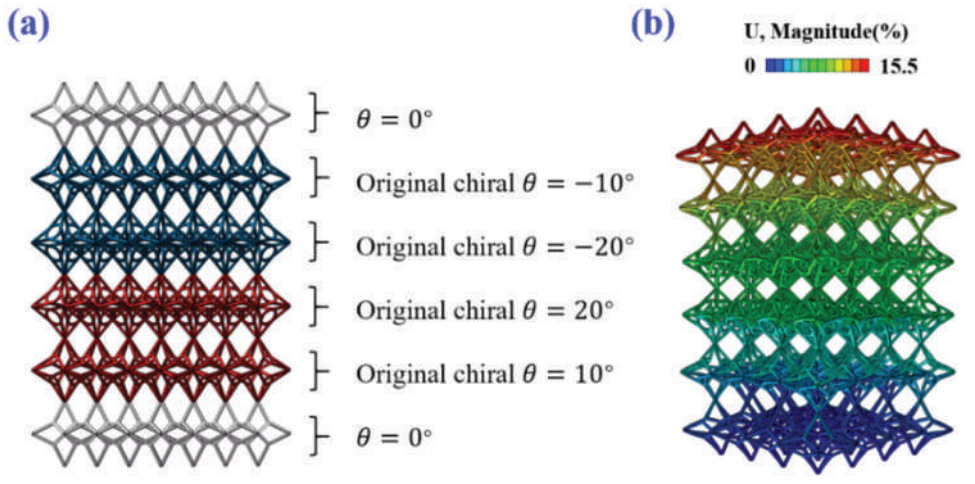

Figure 14. Target metamaterial with specific local deformation. (a) Geometry configuration. (b) The obtained displacement field of the FE model.

$$\varepsilon = \frac{1}{6}\sum_{i=1}^{6}\varepsilon_i = \frac{1}{6}\sum_{i=1}^{6}\frac{\sigma}{E_i} \tag{10}$$

$$\frac{E_{eff}}{E_s} = \frac{\sigma}{\varepsilon}/E_s = 6/E_s\sum_{i=1}^{6}\frac{1}{E_i} = 1.66\times 10^{-4} \tag{11}$$

where ε_i and $E_i (i = 1, \ldots, 6)$ is the strain and Young's modulus of each layer, respectively.

Moreover, the target metamaterial does not exhibit a tension-twist coupling behavior because the assembly direction of the upper and lower layers are opposite, which will offset the overall chirality behavior. However, the local mechanical properties of the target metamaterial vary from layer to layer, as shown in Figure 15. In the middle part of this structure, the target metamaterial exhibits a larger Young's modulus and Poisson's ratio. With the increase of the absolute value of the topological angle, the local tension-twist behavior can be observed. By changing the number of layers, topology parameters and assembly types, specific structures and applications can be obtained.

Utilizing the face-rotating polyhedral (FRP) method, three-dimensional (3D) chiral and anti-chiral metamaterials can be designed, which greatly improves the design efficiency. From the experiment and FEA results, it can be obtained that the 3D chiral and anti-chiral metamaterials assembled by using the two dimensions (2D) chiral structures can deform as intended. Moreover, the mechanical behavior of the structures can be adjusted by changing the topological parameter. Consequently, the abnormal mechanical behavior of the metamaterials can be obtained by changing 2D chiral cells and the topological angle of units.

5. Shape memory

When the temperature is higher than T_g, SMP is in the rubbery state, and the structure has a large deformation capacity. Exemplified by the DS anti-chiral mematerials with $\theta = 10°$,

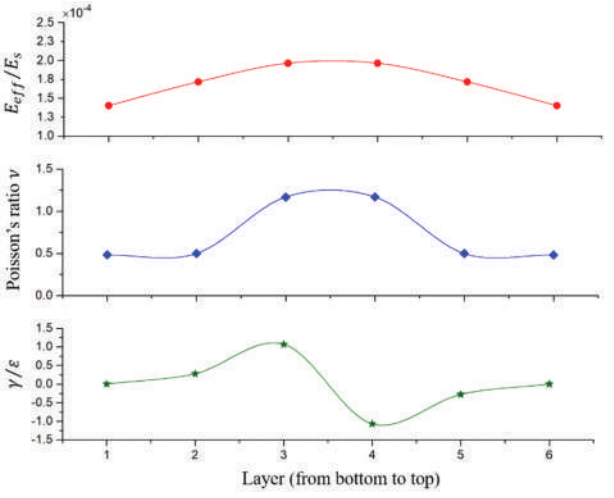

Figure 15. Local mechanical properties of the target metamaterial.

CS anti-chiral metamaterial with $\theta = 30^\circ$ and DS chiral metamaterial with $\theta = 20^\circ$, the thermal-mechanical cycle tests were conducted to investigate the shape memory behavior of the metamaterials. First, the structures were applied 90 mm deformation at 70°C. Second, keep the deformation and lower the temperature to 20°C, then the deformation was memoried. Subsequently, the temperature was heated from 25°C to 100°C with a heating rate of 3°C/min while keeping the load zero. The recovery processes of the deformation with temperature are shown in Figure 16(a), and the shape recovery ratio was about 93%. During the recovery process, the configuration of CS anti-chiral metamaterial with $\theta = 30^\circ$ at different temperatures is shown in Figure 16(b). The shape recovery started at 40°C, and when the temperature was heated to 70°C and 80°C, the deformation recovery was about 70% and 90%. The comparison between simulation and experiment is shown in Figure 16(c). The initially applied deformation was defined as 100%. With the increase in temperature, 95% of the applied deformation recovered. In terms of shape recovery ratio, about 5% of deformation did not recover in both simulation results and experimental results.

6. Conclusions

Inspired by the icosahedral cricket paralysis virus, planar chiral units are assembled into 3D chiral cells, transferring chirality from 2D to 3D. In this work, four kinds of innovative design and assembly of 3D chiral and anti-chiral metamaterials are proposed and fabricated by 3D printing utilizing SMP, including original chiral, DS chiral metamaterials, DS anti-chiral and CS anti-chiral metamaterials. The chiral and anti-chiral metamaterials with different topology parameters are investigated by experiments and FEA to verify the mechanical properties. The results indicated that chiral metamaterials exhibit tension-twist coupling behavior. Combined with programmatic calculations and distributions, target metamaterial with specific local deformation was obtained to achieve some unique applications. The shape recovery experiment indicated the large deformation ability and

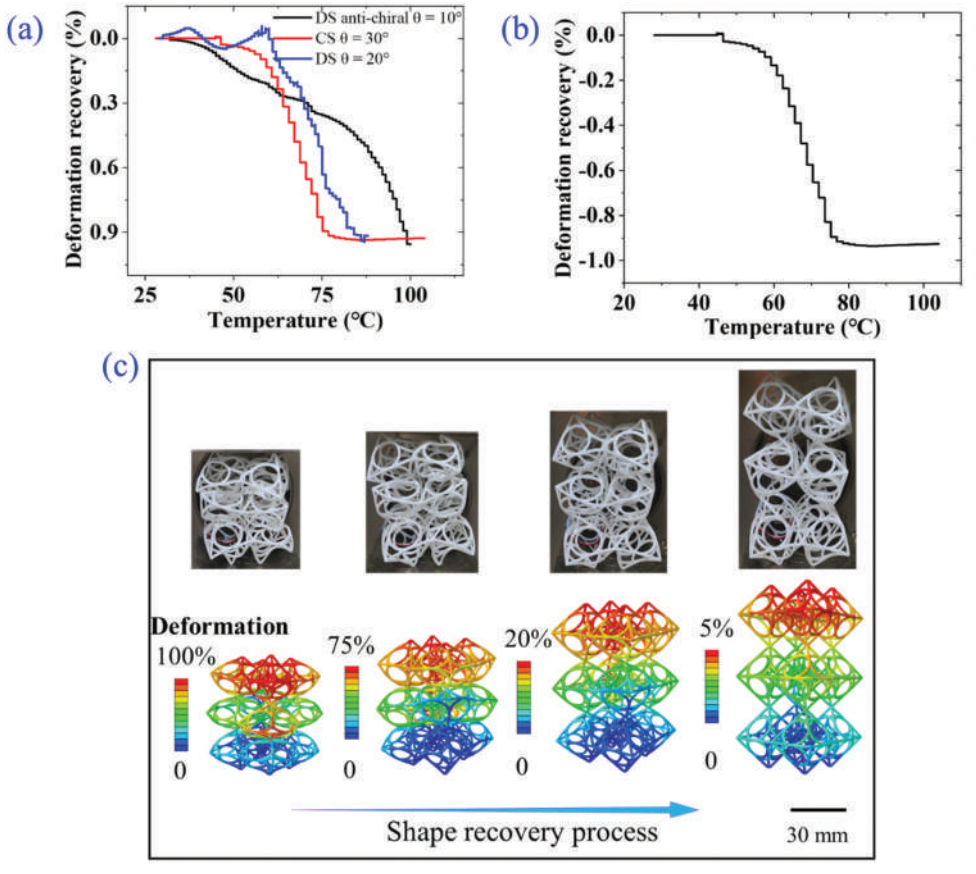

Figure 16. Shape recovery of the metamaterials (a) Deformation recovery vs. temperature (b) Metamaterials configuration at different temperatures during the shape recovery process (c) Comparison between simulation and experiment.

shape memory property of the metamaterials. Both the chiral cells and anti-chiral cells can be obtained by using different assembly methods, which greatly improve design efficiency. This innovative method proves to be feasible and functional, thus it opens a new door for the design of 3D chiral and anti-chiral metamaterials.

Disclosure statement

No potential conflict of interest was reported by the author(s).

Funding

This work was supported by the National Natural Science Foundation of China [Grant No. 12072094 and 12172106], Heilongjiang Touyan Innovation Team Program and the Fundamental Research Funds for the Central Universities [No. IR2021106 and IR2021232]

ORCID

Wei Zhao http://orcid.org/0000-0002-7045-912X
Jinsong Leng http://orcid.org/0000-0001-5098-9871

References

[1] Nimbolkar A, Kumar H, Kumar G. Alternatives to metamaterial based antennas for gain and bandwidth enhancement. IETE J Res. 2021;1–7. DOI:10.1080/03772063.2021.1886878
[2] Mrf A, Sg A, Zv B. Solute concentration sensing in two aqueous solution using an optical metamaterial sensor-ScienceDirect. J Lumin. 2021;230:117734.
[3] Elenk E, Tokan, Turker Tokan N. Frequency scanning conformal sensor based on SIW metamaterial antenna. IEEE Sens J. 2021;21(14):16015–16023.
[4] Vineetha K, Kumar M, Madhav B, et al. Flexible and conformal metamaterial based microwave absorber for WLAN, Wi-MAX and ISM band applications. Mater Technol. 2021 37(8) ;592–609.
[5] Wang H, Yan B, Jin H, et al. Perfect absorber with separated 'dielectric–metal–ground' metamaterial structure. J Phys D Appl Phys. 2021;54(22):225105.
[6] Zhang Y, Yi Z, Wang X, et al. Dual band visible metamaterial absorbers based on four identical ring patches. Physica E. 2020;127:114526.
[7] Vellucci S, Monti A, Barbuto M, et al. Progress and perspective on advanced cloaking metasurfaces: from invisibility to intelligent antennas. EPJ Appl Metamateria. 2021;8(7).
[8] Chen P, Haberman M, Ghattas O. Optimal design of acoustic metamaterial cloaks under uncertainty. J Comput Phys. 2021;431:110114.
[9] Malléjac M, Merkel A, Sánchez-Dehesa J, et al. Experimental evidence of a hiding zone in a density-near-zero acoustic metamaterial. J Appl Phys. 2021;129(14):145101.
[10] Hajati Y, Marbouieh S, Sabaeian M. Tunable far-infrared hyperbolic metamateial based on graphene-polar dielectric. Physica E. 2020;128:114534.
[11] Boccaccio M, Fierro G, Bucciarelli F, et al. Multi-tonal subwavelength metamaterial for absorption and amplification of acoustic and ultrasonic waves. Eng Res Exp. 2021;3(2):025024.
[12] Wang J, Lang T, Hong Z, et al. Design and fabrication of a triple-band terahertz metamaterial absorber. Nanomaterials. 2021;11(5):1110.
[13] Xin X, Liu L, Liu Y, et al. 4D printing auxetic metamaterials with tunable, programmable, and reconfigurable mechanical properties. Adv Funct Mater. 2020;30:2004226.
[14] Mizzi L, Salvati E, Spaggiari A, et al. 2D auxetic metamaterials with tuneable micro-/nanoscale apertures. Appl Mater Today. 2020;20:100780.
[15] Raghunath G, Flatau A, Wang H, et al. Magnetoelastic auxetic-like behavior in Galfenol: experimental data and simulations. Phys Status Solidi B. 2016;253(7):1440–1448.
[16] Fb A, Cgj B, Pp A. Hard auxetic metamaterials. Extreme Mech Lett. 2020;40:100980.
[17] Ren X, Das R, Tran P, et al. Auxetic metamaterials and structures: a review. Smart Mater Struct. 2018;27(2):023001.
[18] Saxena K, Das R, Calius E. Three decades of auxetics research-materials with negative Poisson's ratio: a review. Adv Eng Mater. 2016;18(11):1847–1870.
[19] Shen J, Zhou S, Huang X, et al. Simple cubic three-dimensional auxetic metamaterials. Phys Status Solidi B. 2014;251(8):1515–1522.
[20] Ren X, Shen J, Ghaedizadeh A, et al. Experiments and parametric studies on 3D metallic auxetic metamaterials with tuneable mechanical properties. Smart Mater Struct. 2015;24(9):095016.
[21] Ren X, Shen J, Tran P, et al. Design and characterisation of a tuneable 3D buckling-induced auxetic metamaterial. Mater Design. 2018;139:336–342.
[22] Novak N, Vesenjak M, Ren Z. Auxetic cellular materials-a review. Stroj vestn-J Mech E. 2016;62(9):485–493.
[23] Prall D, Lakes R. Properties of a chiral honeycomb with a Poisson's ratio of −1. Int J Mech Sci. 1997;39(3):305–314.

[24] Liu X, Huang G, Hu G. Chiral effect in plane isotropic micropolar elasticity and its application to chiral lattices. J Mech Phys Solids. 2012;60(11):1907–1921.
[25] Frenzel T, Kadic M, Wegener M. Three-dimensional mechanical metamaterials with a twist. Science. 2017;358(6366):1072–1074.
[26] Duan S, Wen W, Fang D. A predictive micropolar continuum model for a novel three-dimensional chiral lattice with size effect and tension-twist coupling behavior. J Mech Phys Solids. 2018;121:23–46.
[27] Ha C, Plesha M, Lakes R. Chiral three-dimensional lattices with tunable Poisson's ratio. Smart Mater Struct. 2016;25(5):054005. .
[28] Qi D, Zhang P, Wu W, et al. Innovative 3D chiral metamaterials under large deformation: theoretical and experimental analysis. Int J Struct. 2020;202:787–797.
[29] Mizzi L, Spaggiari A. Chiralisation of Euclidean polygonal tessellations for the design of new auxetic metamaterials. Mech Mater. 2021;153(80):103698.
[30] Mizzi L, Spaggiari A. Novel chiral honeycombs based on octahedral and dodecahedral Euclidean polygonal tessellations. Int J Struct. 2022;238:111428.
[31] Tarnai T, Fowler P, Guest S, et al. Equiauxetic hinged archimedean tilings. Symmetry. 2022;14:232.
[32] Wu W, Qi D, Liao H, et al. Deformation mechanism of innovative 3D chiral metamaterials. Sci Rep. 2018;8(1):12575.
[33] Wu W, Hu W, Qian G, et al. Mechanical design and multifunctional applications of chiral mechanical metamaterials: a review. Mater Design. 2019;180:107950.
[34] Zhao W, Zhu J, Liu LW, et al. Analysis of small-scale topology and macroscale mechanical properties of shape memory chiral-lattice metamaterials. Compos Struct. 2021;262:113569.
[35] Wang X, Wang Y, Yang H, et al. Assembled molecular face-rotating polyhedra to transfer chirality from two to three dimensions. Nat Commun. 2016;7:12469.
[36] Yeung C, Yim K, Wong H, et al. Chiral transcription in self-assembled tetrahedral Eu_4L_6 chiral cages displaying sizable circularly polarized luminescence. Nat Commun. 2017;8(1):1128.
[37] Zhao W, Huang Z, Liu L, et al. Bionic design and performance research of tracheal stent based on shape memory polycaprolactone. Compos Sci Technol. 2022;229(): 109671.
[38] Zhao W, Zhang F, Leng J, et al. Personalized 4D printing of bioinspired tracheal scaffold concept based on magnetic stimulated shape memory composites, Compos. Sci Technol. 2019;184:107866.
[39] Zhang F, Wen N, Wang L, et al. Design of 4D printed shape-changing tracheal stent and remote controlling actuation. Int J Smart Nano Mat. 2021;12(4):375–389.
[40] Zhao F, Zheng X, Zhou S, et al. Constitutive model for epoxy shape memory polymer with regulable phase transition temperature. Int J Smart Nano Mat. 2021;12(1):72–87.
[41] Zhao W, Huang Z, Liu L, et al. Porous bone tissue scaffold concept based on shape memory PLA/Fe_3O_4. Compos Sci Technol. 2021;205:108563.
[42] Zhao W, Liu L, Leng J, et al. Thermo-mechanical behavior prediction of shape memory polymers based on multiplicative decompositions of the deformation gradient. Mech Mater. 2020;143:103263.
[43] Zhao W, Liu L, Leng J, et al. Thermo-mechanical behavior prediction of carbon nanotube reinforced shape memory polymer composite. Compos Part B-Eng. 2019;179:107455.
[44] Zhao W, Li N, Liu L, et al. Origami derived self-assembly stents fabricated via 4D printing. Compos Struct. 2022;293:115669.